

# Accurate Surface and Reflectance Modelling from 3D Radar Data with Neural Radiance Fields

Judith Treffler, Vladimír Kubelka, Henrik Andreasson, Martin Magnusson

**Abstract**—Robust scene representation is essential for autonomous systems to safely operate in challenging low-visibility environments. Radar has a clear advantage over cameras and lidars in these conditions due to its resilience to environmental factors such as fog, smoke, or dust. However, radar data is inherently sparse and noisy, making reliable 3D surface reconstruction challenging. To address these challenges, we propose a neural implicit approach for 3D mapping from radar point clouds, which jointly models scene geometry and view-dependent radar intensities. Our method leverages a memory-efficient hybrid feature encoding to learn a continuous Signed Distance Field (SDF) for surface reconstruction, while also capturing radar-specific reflective properties. We show that our approach produces smoother, more accurate 3D surface reconstructions compared to existing lidar-based reconstruction methods applied to radar data, and can reconstruct view-dependent radar intensities. We also show that in general, as input point clouds get sparser, neural implicit representations render more faithful surfaces, compared to traditional explicit SDFs and meshing techniques.

## I. INTRODUCTION

Accurate and reliable representations of the environment are essential for autonomous systems, particularly in low-visibility conditions. However, classical explicit mapping approaches often struggle with sparse or noisy data. In the last few years, neural implicit scene representations, such as Neural Radiance Fields (NeRF) [1], have become a widely adopted framework for 3D mapping [2], [3], [4]. Unlike explicit representations, which employ fixed spatial data structures, neural methods implicitly represent the surface structure with a neural network and trainable features, enabling maps with improved surface reconstruction at arbitrary resolutions. Still, the majority of these methods focus on camera or lidar data and might fail in low-visibility environments. Radar, with its ability to penetrate clouds of small particles such as fog, smoke, or dust with minimal attenuation, is a promising alternative. The view-dependent intensities and reflections of radar data can provide valuable information for localisation and scene understanding. However, radar also introduces additional challenges, as the noisy data – particularly multi-path reflections – makes accurate modelling more difficult.

Despite its potential, radar-based neural implicit scene representations have remained unexplored until recently. Existing methods focus on 2D novel view synthesis (NVS) with limited 3D reconstruction [5], [6], [7], perform NVS of 3D radar

\*This work was partially supported by the Wallenberg AI, Autonomous Systems and Software Program (WASP) funded by the Knut and Alice Wallenberg Foundation.

The authors are with ARC and the AASS RNP lab, Örebro University, Sweden {judith.treffler, vladimir.kubelka, henrik.andreasson, martin.magnusson}@oru.se

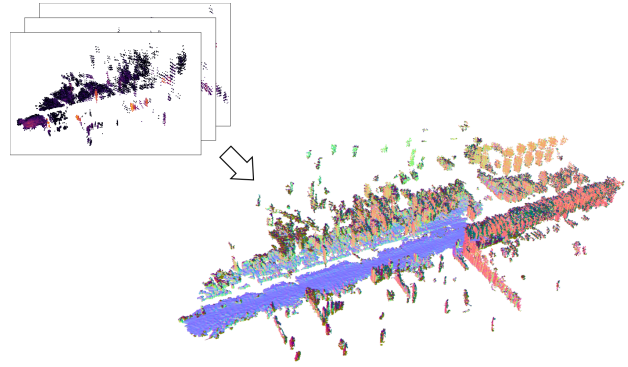


Fig. 1: Accurate surface reconstruction (right) produced by 3QFPI from a set of 3D radar point clouds (left) from the Radar Forest dataset. The mesh is coloured according to surface normals.

point clouds via projections to 2D range maps [8], or can only model radar jointly with camera and lidar [9]. To the best of our knowledge, no prior work has reconstructed 3D surfaces from radar point clouds while modelling view-dependent radar intensities.

In this paper, we propose a neural implicit approach for 3D mapping from radar point clouds that offers both accurate surface reconstruction and modelling of view-dependent intensities. We base our method on the memory-efficient 3QFP representation, designed for dense lidar point clouds [4], and learn a Signed Distance Field (SDF) for surface reconstruction directly from 3D radar data. Inspired by the architecture of NeuS2 [10], we introduce an intensity network that models view-dependent radar intensities, enabling our method to learn both geometric and reflective aspects from radar data. This network can implicitly account for sensor-specific constants of the radar equation, such as transmitted power and antenna gain. We further analyse the impact of the components of the NeuS2 architecture on the intensity reconstruction quality when applied to radar data.

Our main contributions are as follows:

- A memory-efficient learnable radar reflectivity model that accounts for surface geometry and view-dependent backscatter, improving reconstruction quality and robustness in low-visibility and feature-poor environments.
- An evaluation of 3D reconstruction methods on two radar sensors with different noise characteristics.
- A discussion on metrics for assessing radar-based environment modelling.

As our experiments demonstrate, our approach produces

more accurate surface reconstructions with smoother locally planar regions from radar data, compared to both classical explicit methods and recent neural representations, while also predicting realistic view-dependent radar intensities across varying viewing angles.

## II. RELATED WORK

3D mapping has traditionally relied on explicit scene representations, such as occupancy grids [11], [12], surfels [13], [14], meshes [15], [16], [17], [18], [19] or Truncated Signed Distance Field (TSDF) values [20], [21]. These discretised spatial representations often face challenges with scalability, memory inefficiency at high resolutions, and reconstruction of fine details or unobserved areas. In the last few years, neural implicit methods have gained popularity. In contrast to explicit approaches, they use multi-layer perceptrons (MLP) to learn a continuous scene representation, enabling reconstruction at different resolutions, improved completion, and more robustness to sparse input data. The seminal work introducing Neural Radiance Fields (NeRF) [1] learns a volumetric scene representation from 2D images. While intended for novel view synthesis, scene geometry can be extracted via volume rendering; however, since surface geometry is inferred from the volume density field, high-quality surface extraction remains challenging, and often results in noisier reconstructions.

To learn surface representations more directly, several approaches learn implicit occupancy fields [22], [23], [24] or signed distance functions [25]. In particular, NeuS [26] and its extension NeuS2 [10] combine volume rendering with an SDF and use a separate network to model view-dependent components. Beyond camera-based methods, SHINE-Mapping [3] and 3QFP [4] learn an SDF from lidar data. SHINE-Mapping uses an octree-based data structure to store learnable features. Building on this, 3QFP reduces the memory usage while maintaining the reconstruction quality by replacing octrees with more efficient tri-quadtrees and using Fourier feature positional encoding. Neural implicit scene representations have further been applied to other sensors, including ultrasound [27], sonar [28], [29], or synthetic aperture radar (SAR) [30], [31].

Most neural implicit reconstruction methods focus on RGB, RGB-D, lidar, or combinations thereof and might fail in low-visibility environments. While several advances have been made to overcome these challenges [32], [33], radar offers an inherently more robust solution. Its longer wavelength enables radar signals to penetrate clouds of small particles (dust, smoke, fog, etc.) with little attenuation, making it well-suited for low-visibility conditions without specialised correction techniques. For autonomous systems, two types of mmWave radar sensors are commonly used: spinning radars that capture 2D polar images, or system-on-a-chip (SoC) radars that generate 3D radar data cubes with an additional velocity dimension, often referred to as 3+1D or 4D radar.

Despite these advantages, the sparse and noisy nature of radar data poses challenges for neural implicit representations, which have only recently been explored. Initial work with 2D

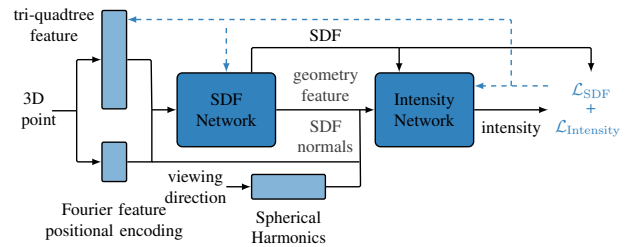


Fig. 2: **Network Architecture:** Given a 3D point  $\mathbf{x}$ , we concatenate its tri-quadtree feature and Fourier feature positional encoding and pass them to the SDF network. The SDF network predicts an SDF value and, optionally, a learned geometry feature and/or approximated SDF normals. These outputs, along with the spherical harmonics-encoded viewing direction and the Fourier feature encoding of  $\mathbf{x}$ , are concatenated and fed into the intensity network to predict the intensity value for  $\mathbf{x}$ .

radars consists of DART [6], which performs NVS on range-Doppler radar images. Radar Fields [5] and RF4D [7] perform NVS and 3D mapping from 2D radar data, and thus are limited in elevation and detail. For 3D radar, GeoRF [8] reconstructs and refines point clouds, but relies on learning 2D range maps from down-projected 3D data, which can lead to information loss. NeuRadar [9] jointly models camera, lidar, and 3D radar data for NVS, but cannot operate using radar alone. To the best of our knowledge, no existing work reconstructs surfaces from only radar point clouds. Furthermore, while Radar Fields and RF4D model 2D radar reflectance and combine it with occupancy for NVS, modelling radar intensities has not yet been extended to 3D radar data. Since radar reflections encode view-dependent and material-specific properties, explicitly modelling intensities provides complementary information to the reconstructed geometry.

## III. METHOD

We model the scene geometry by learning a continuous SDF and view-dependent radar intensities with an SDF and an intensity network. The weights of both networks, together with feature vectors that are stored in a memory-efficient tri-quadtree grid, are jointly optimised using radar range detections and intensities from known sensor poses. The learned SDF allows for mesh reconstruction using marching cubes [34], while the intensity network can be queried at arbitrary 3D points and viewing directions to reconstruct view-dependent radar intensities. We will refer to our architecture as 3QFPI (3QFP with intensities).

### A. Network

Inspired by NeuS2 [10], which models view-dependent colours using separate geometry and RGB networks, our network architecture consists of an SDF network that models scene geometry and an intensity network that predicts view-dependent radar intensities. The intensity network is conditioned on the scene geometry learned by the SDF network. Figure 2 shows an overview of the architecture.

1) *SDF Network*: We use 3QFP [4] as our SDF network due to its memory-efficient but powerful hybrid feature encoding. 3QFP encodes each 3D point with tri-quadtrees, by projecting a 3D point  $\mathbf{x}$  onto three axis-aligned orthogonal planes, and constructing a quadtree on each plane. Nodes at the deepest  $H$  levels of a quadtree contain learnable feature vectors for interpolation. These vertex features are stored in hash tables to enable fast queries. The learnable tri-quadtree feature encoding is combined with Fourier feature positional encoding, creating a hybrid representation that produces smoother results and improves the completion, with only a minimal increase in computational cost [4]. For further details on 3QFP’s architecture, we refer to the original paper [4].

To integrate 3QFP into the NeuS2 architecture, we modify the network to optionally output a geometry feature vector  $\mathbf{g} \in \mathbb{R}^{15}$  and SDF normals  $\mathbf{n}$ , alongside the SDF value  $d$ . The geometry feature and the normals, calculated as the gradients of the SDF  $\mathbf{n} = \nabla_{\mathbf{x}}d$ , provide additional geometric information to the intensity network. Both outputs are optional, as our ablation study (section IV-C.2) showed minimal effect on intensity reconstruction.

2) *Intensity Network*: Our intensity network predicts the radar return at a 3D point in space, given a viewing direction. According to the radar equation,

$$P_r = \frac{P_t G_t A_{\text{eff}} \sigma}{(4\pi)^2 r^4} \quad (1)$$

the received intensity depends on the distance and object properties. The transmitted power  $P_t$ , signal gain  $G_t$ , and effective area of the receiver  $A_{\text{eff}}$  are constant for all detected objects. If the manufacturer provides the information, these constants are known; otherwise, the network can learn them implicitly. The radar cross section  $\sigma$  depends on the incident angle (viewing direction), angle of reflection, material and object size, and can be inferred from the scene geometry or learned implicitly.

The intensity network takes the 3D point  $\mathbf{x}$ , the viewing direction  $\mathbf{v}$ , the SDF value  $d$ , and optionally the geometry feature  $\mathbf{g}$  and SDF normals  $\mathbf{n}$  as input. Consistent with the SDF network, we encode  $\mathbf{x}$  with Fourier feature positional encoding, while  $\mathbf{v}$  is encoded with Spherical Harmonics. The SDF value, geometry feature, and normal provide geometry information and thus indirectly describe the detected objects’ shape and angle of reflection. From these inputs, the intensity network predicts the radar intensity at  $\mathbf{x}$  when seen from  $\mathbf{v}$ .

## B. Training

1) *Sampling*: We adopt the sampling process from 3QFP, sampling both near the input radar points and in free space. For every input point  $\mathbf{x}$ , we randomly sample  $N_s$  points along the ray near  $\mathbf{x}$ , and  $N_f$  points along the ray in free space between the sensor and  $\mathbf{x}$ . Both SDF and intensity labels are assigned to the same sampled points. The SDF-labels are set as the signed distance between the sampled point and  $\mathbf{x}$ . Samples between the sensor and  $\mathbf{x}$  are assigned negative labels; samples beyond  $\mathbf{x}$  have positive labels. For the intensity labels, we assign the same intensity as the ground

truth point to the samples near  $\mathbf{x}$ , assuming local intensities are approximately constant due to the low spatial resolution of radar. We normalise the ground truth intensities to the range [0,1] to compensate for sensor-specific thresholding. Since we do not expect a radar return in free space, we set the label of free-space samples to 0.

2) *Loss Function*: The loss function consists of an SDF component and an intensity component. For the SDF loss, we follow SHINE-Mapping and 3QFP [3], [4]: We first map the SDF value to [0,1] with a sigmoid function and then use a Binary Cross-Entropy loss. This gives sample points close to the surface a higher impact and allows faster convergence. Like 3QFP, we do not include additional SDF regularisation, Eikonal or loss weight terms, since they did not noticeably affect the reconstruction. For the intensity loss, we use an L1 loss, which was experimentally found to achieve more accurate results than an L2 loss, presumably because it is less sensitive to outliers in sparse, noisy radar data.

## IV. EXPERIMENTS

### A. Experiment Setup

1) *Surface Reconstruction Baselines*: We compare our surface reconstruction to meshes created with classical mesh generation methods:  $\alpha$ -shapes [15], Ball-Pivoting Algorithm (BPA) [16], and Poisson Surface Reconstruction (Poisson) [17]. Additionally, we evaluate against VDBFusion [21], a TSDF-based explicit scene reconstruction method, and SHINE-Mapping [3], a lidar-based neural implicit mapping approach that learns an SDF.

2) *Evaluation Metrics*: We evaluate the surface reconstruction quality following the setup and thresholds from [3], [4] by uniformly sampling  $10^7$  points on each mesh and calculating the *accuracy* and *completion errors*. The *accuracy error* is the average minimum distance from the mesh samples to ground truth lidar points, discarding distances above 0.4 m. We additionally report the percentage of discarded distances as the *accuracy outlier ratio*. The *completion error* is computed as the average minimum distance from ground truth points to the mesh samples, with distances truncated at 2.0 m. Lidar point clouds are used as ground truth, since they are denser and less noisy than radar data. We also report the *accuracy* and *completion ratio*, and *F-score* as the percentage of errors below a threshold of 0.2 m. To account for the different fields of view and ranges of radar and lidar, we manually restrict the evaluation to the bounding box where both sensors overlap and have high point density.

The distance thresholds applied in the evaluation can substantially affect the results. In particular, discarding larger distances in the accuracy calculation can make meshes with strong interpolation in unobserved areas appear overly accurate. We report the aforementioned metrics for comparison with lidar-based reconstructions, but note that they do not fully capture reconstruction quality for sparser radar data.

To assess reconstruction of locally planar surfaces from noisy data, we fit a Gamma distribution to the histogram of angles between adjacent triangles (see fig. 4), reporting

TABLE I: Quantitative evaluation of the surface reconstruction quality on the Radar Forest and SNAIL-Radar dataset using lidar point clouds as ground truth. We compare accuracy and completion errors (m), and accuracy ratio, completion ratio and F-score (%) with a threshold of 0.2 m. Distances above 0.4 m are omitted from the accuracy calculation, and the accuracy outlier ratio is additionally reported. To assess local planarity of surfaces, we evaluate the shape, mean, and variance of the Gamma distribution fitted to the histogram of angles between adjacent triangles (see fig. 4). Overall, 3QFPI achieves the best accuracy and preserves planar surface patches, while Poisson and SHINE-Mapping achieve the best completion. The best results per metric are highlighted in **bold**.

dataset	method	Acc.	Acc.	Acc. Out.	Comp.	Comp.	F-Score (%) $\uparrow$	Gamma	Gamma	Gamma
		Error (m) $\downarrow$	Ratio (%) $\uparrow$	Ratio (%) $\downarrow$	Ratio (%) $\uparrow$	Error (m) $\downarrow$		Shape	Mean $\downarrow$	Variance $\downarrow$
Radar Forest	$\alpha$ -shapes	0.1566	65.4061	37.4796	0.3095	66.2153	65.8082	1.3492	0.8628	0.5517
	BPA	0.1595	64.9883	34.2065	0.3493	61.3386	63.1107	1.7484	0.6517	0.2429
	Poisson	0.1590	65.0666	48.9905	<b>0.2518</b>	<b>74.6448</b>	69.5274	1.0930	0.4861	0.2162
	VDBFusion	0.1493	69.1786	<b>23.8463</b>	0.4076	55.7333	61.7323	1.2013	0.5367	0.2398
	SHINE	0.1480	69.3238	32.1037	0.3170	66.4165	67.8390	1.2727	0.5336	0.2237
	3QFPI	<b>0.1336</b>	<b>73.6180</b>	26.1608	0.3453	66.2283	<b>69.7279</b>	0.7239	<b>0.3103</b>	<b>0.1330</b>
SNAIL-Radar	$\alpha$ -shapes	0.1807	59.2408	61.4282	0.3086	50.2208	54.3592	2.2448	1.2221	0.6653
	BPA	0.1679	63.5739	45.1021	0.3894	44.2758	52.1983	1.8124	0.6918	0.2640
	Poisson	0.1751	61.1234	59.2611	0.1819	<b>76.2889</b>	67.8693	1.1437	0.5220	0.2382
	VDBFusion	<b>0.1676</b>	63.7774	<b>44.6304</b>	0.3352	56.8112	60.0931	1.5202	0.6722	0.2972
	SHINE	0.1713	62.7132	50.6683	<b>0.1713</b>	75.9790	<b>68.7117</b>	1.4209	0.5918	0.2465
	3QFPI	<b>0.1676</b>	<b>64.5685</b>	45.5781	0.4672	41.5644	50.5734	0.9098	<b>0.4352</b>	<b>0.2081</b>

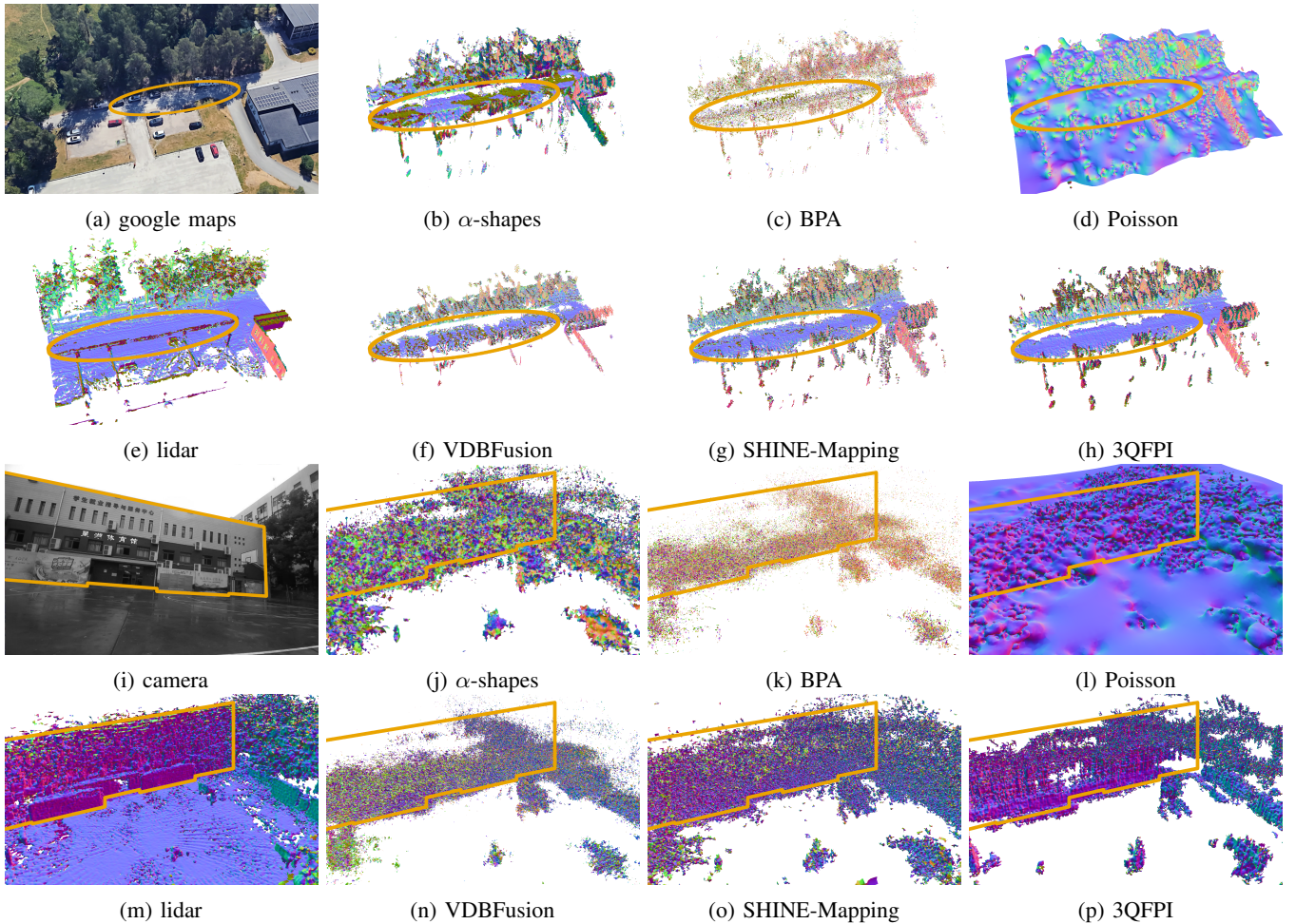


Fig. 3: Surface reconstruction quality of different methods on the Radar Forest dataset (a–h), and a corner of the SNAIL-Radar basketball court dataset showing a basket and a building in the background (i–p). For reference, we include an image of the scene (from a different angle) and the lidar-based reconstruction created with SHINE-Mapping; meshes are coloured by surface normals. The comparison indicates that 3QFPI produces more accurate and smoother locally planar surfaces from noisy data. In particular, the reconstruction of the building in (p) is closest to the lidar reference (m).

shape, mean, and variance in table I. Lower mean and variance indicate smoother surface patches, while lower shape values correspond to distributions concentrated near zero with a long tail of larger angles at edges or sharp features. We note that these metrics are supplementary and should be considered alongside previously described metrics and qualitative evaluation, as their interpretation depends on the scene. In environments like the ones in our datasets, where a majority of the surfaces are planar, lower mean and variance should correspond to higher-quality reconstructions.

To evaluate the predicted intensities, we hold out every tenth point cloud during training and compare the reconstructed intensities to the ground truth using the Mean Absolute Error (MAE) and Median Absolute Error (MedAE) in table II, table III, and fig. 7.

3) *Datasets*: We evaluate our method on three different outdoor radar datasets: 1) the Radar Forest dataset<sup>1</sup> using data labeled "bag0" (Hugin A3, 48Tx/48Rx antennas); 2) the publicly available SNAIL-Radar dataset [35], using the denser AI-enhanced radar point clouds from sequence 20231007/4 and 20231208/1 (Oculii Eagle, 6Tx/8Rx antennas); and 3) a dataset specifically recorded to assess view-dependent intensity recovery, collected by moving the sensor in a semicircle around a corner reflector mounted on a wall to capture measurements at varying incidence angles and approximately constant range (Hugin A4, 48Tx/48Rx antennas).

We remove points within a 2.5 m radius (1 m for SNAIL-Radar) around the sensor to suppress near-field clutter and densify point clouds by accumulating five consecutive frames.

4) *Implementation*: We implement the classical surface reconstruction methods using Open3D [36], setting parameters to achieve reasonable performance on our datasets:  $\alpha$ -shapes with  $\alpha = 0.2$ ; BPA with a pivoting radius of 0.1 m; and Poisson with an octree depth of 12. For VDBFusion, we set the voxel size to 0.2 m and enable isolated vertex filtering. SHINE-Mapping and 3QFPI use a leaf node resolution of 0.2 m. For mesh extraction and rendering of VDBFusion, SHINE-Mapping, and 3QFPI, we use a voxel size of 0.1 m. In 3QFPI, we increase the number of free-space and near-surface samples to 6 to improve completion, train for 4000 iterations with a learning rate of  $10^{-3}$ , and freeze the SDF network after 1000 iterations. We normalise intensities using the rounded dataset-wide minimum and maximum.

## B. Surface Reconstruction Experiment Results

1) *Surface Reconstruction with Dense Input Data*: We first evaluate the surface reconstruction using all frames of each dataset. Table I shows that 3QFPI achieves the lowest accuracy error and highest accuracy ratio on both datasets, indicating close geometric alignment with the lidar ground truth. While VDBFusion yields a slightly lower accuracy outlier ratio due to its sparser reconstruction, 3QFPI preserves more radar details but also artefacts, which increase the

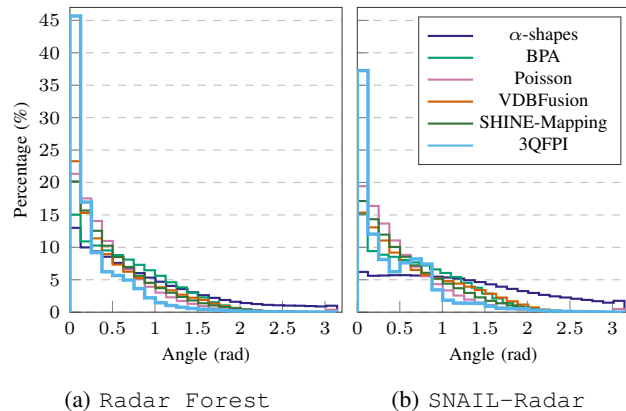


Fig. 4: Outlines of the histograms of angles between adjacent mesh triangles for surface reconstructions from the Radar Forest and SNAIL-Radar datasets. For both datasets, 3QFPI produces the largest proportion of small angles, indicating better preservation of locally planar regions, such as at the ground or walls.

outlier count. Poisson surface reconstruction achieves the highest completion ratio and competitive F-score; however, the reconstructions are overly smooth (see figs. 3d and 3l), as the method fills unobserved areas to generate watertight surfaces. This interpolation can introduce geometrically incorrect regions and lead to a high outlier rate. SHINE-Mapping achieves high completion and accuracy, but preserves more radar details and noise, also resulting in an increased outlier ratio.

The qualitative evaluation with SNAIL-Radar data in fig. 3 indicates that a high F-score does not necessarily correspond to a geometrically accurate reconstruction. Since mesh samples more than 0.4 m from the nearest ground truth point are excluded from the accuracy calculation – as in SHINE-Mapping and 3QFP [3], [4] – reconstructions with a high outlier ratio can still achieve high F-scores. This effect seems more pronounced in radar-based reconstruction, due to the sparse and noisy data. As a result, both Poisson and SHINE-Mapping achieve high F-scores, while their overly smooth or noisy reconstructions obscure details, such as the building or the basketball goal (see figs. 3l and 3o). In contrast, 3QFPI tends to extract planar surfaces, such as the ground or building facades, more reliably from noisy data, producing meshes that are more consistent with the lidar reference in planar areas. This observation is supported by the distribution of angles between adjacent triangles in the mesh (see fig. 4), where 3QFPI yields the most angles close to zero for both datasets. As table I shows, the fitted Gamma distribution further quantifies this behaviour: 3QFPI produces the lowest mean and variance, indicating smoother and more homogeneous local surface regions, and a lower shape parameter, reflecting more nearly coplanar triangles, with sharper angles confined to fewer regions, e.g., at edges.

2) *Surface Reconstruction with Sparse Input Data*: We evaluate robustness to sparse input using every  $n^{\text{th}}$  point cloud from the Radar Forest dataset as input. As shown

<sup>1</sup>Dataset under review, available at [https://anonymous.4open.science/r/radar\\_forest\\_dataset-0442](https://anonymous.4open.science/r/radar_forest_dataset-0442)

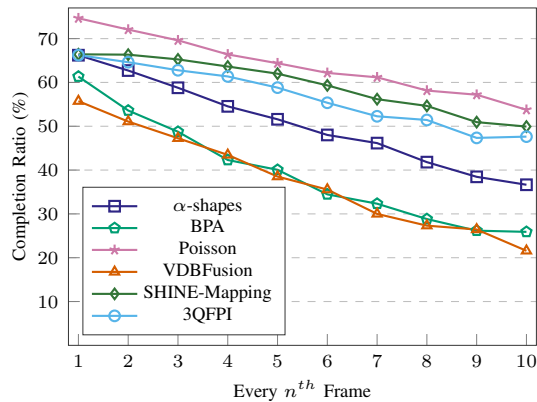


Fig. 5: Comparison of completion ratios using every  $n^{\text{th}}$  point cloud from the Radar Forest dataset as input. Except for Poisson, the completion of classical meshing methods declines quickly with sparse input, whereas neural implicit methods remain more robust.

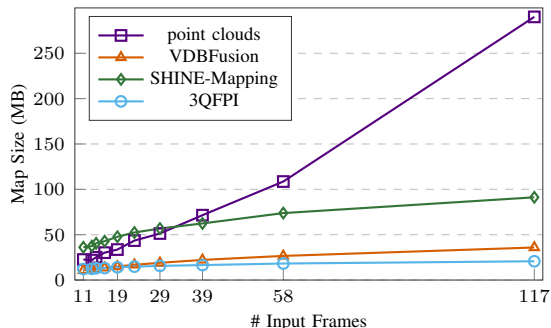


Fig. 6: Comparison of memory usage for the Radar Forest dataset. 3QFPI has the lowest memory usage, needing only about 20 – 30% of the map size of SHINE-Mapping; however, SHINE-Mapping captures more fine details.

in fig. 5, Poisson consistently achieves the highest completion ratios across all sparsity levels, due to its watertight surfaces that interpolate unobserved areas. However, as this interpolation can over-smooth surfaces, high completion does not necessarily reflect reconstruction quality. The completion of other classical meshing approaches declines more rapidly. In contrast, the neural implicit methods SHINE-Mapping and 3QFPI remain more robust to sparse input, likely because the continuous scene representation can infer unobserved regions.

3) *Memory Usage*: We compare the memory usage of the different maps to that of point clouds. Following [4], we use the stored network parameters as the map size for SHINE-Mapping and 3QFPI, and the VDB structure storing TDSF values for VDBFusion. As fig. 6 shows, 3QFPI has the lowest memory usage, increasing only slightly with the number of input frames due to its efficient tri-quadtrees representation. In contrast, dense point cloud maps require the most memory. While 3QFPI achieves a completion ratio comparable to SHINE-Mapping on the Radar Forest dataset, it requires considerably less memory, likely because SHINE-Mapping

TABLE II: Evaluation of intensity reconstruction quality. We report the MAE and MedAE averaged over 10 repetitions and standard deviations in different scenes with and without view-dependent intensities. The errors are expressed in the same scale as the radar’s intensity measurements. The low errors relative to the sensor’s dynamic range indicate that our method reliably reconstructs view-dependent intensities.

dataset	MAE ( $\pm$ SD)	MedAE ( $\pm$ SD)	intensity range
Radar Forest	3.27 ( $\pm$ 0.06)	2.40 ( $\pm$ 0.05)	64–118
wall w/ window 1	2.65 ( $\pm$ 0.02)	2.00 ( $\pm$ 0.01)	80–138
wall w/ window 2	2.48 ( $\pm$ 0.01)	1.81 ( $\pm$ 0.01)	80–128
wall w/o window	2.81 ( $\pm$ 0.05)	2.09 ( $\pm$ 0.03)	80–133
SNAIL basketball court	4.92 ( $\pm$ 0.05)	2.73 ( $\pm$ 0.06)	0–35
SNAIL starlake tower	4.35 ( $\pm$ 0.14)	2.65 ( $\pm$ 0.08)	0–36

stores features in a hierarchical octree structure and reconstructs more noise and fine details. Compared to VDBFusion, 3QFPI reconstructs more geometric details (see fig. 3), with slightly lower memory usage.

### C. Intensity Reconstruction Experiment Results

1) *Intensity Reconstruction Quality*: To evaluate the intensity reconstruction quality of 3QFPI, we compare the predicted intensities of test frames – held out during training – to the corresponding ground truth point clouds. The errors are reported in the same scale as the sensor’s intensity measurements. As table II shows, our method predicts intensities with small errors relative to the dynamic range of the sensor, even for view-dependent intensities. (MAE around 3 relative to an intensity range of around 50 for the Hugin radar in Radar Forest and the view-dependent data, and MAE around 5 in a range of 35 for the Oculii radar in SNAIL.) Figure 7 illustrates this; our method accurately predicts the decrease in intensity with lower incident angles. However, the higher reconstruction errors for the SNAIL-Radar datasets indicate that the reliability of the prediction depends on the quality of the sensor data.

2) *Ablation Study*: We analyse the impact of different inputs to the intensity network on reconstruction quality by removing the SDF network, the SDF normals, and the geometry feature. Table III shows that training the intensity network alone leads to higher reconstruction errors, emphasising the importance of learning scene geometry separately. However, omitting the SDF normals or geometry feature has only a minor effect, suggesting that 3D radar data, unlike RGB images, already provides sufficient geometric context for view-dependent intensity estimation.

## V. CONCLUSION

In this paper, we present 3QFPI, a neural implicit approach for 3D scene reconstruction from radar point clouds that jointly models geometry and view-dependent radar intensities. Experiments with two radar sensors indicate that neural implicit representations in general are particularly well suited for 3D mapping from sparse and noisy radar data, compared to explicit SDF or meshing techniques. Despite the low spatial

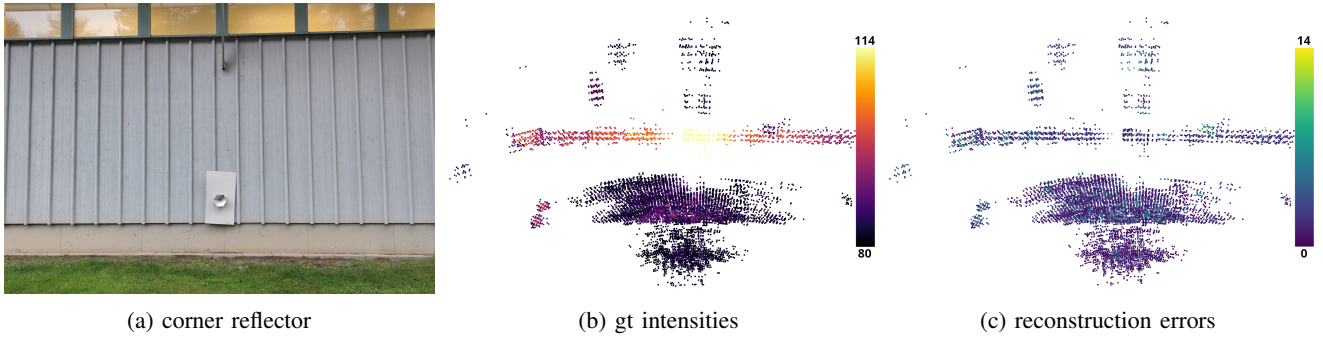


Fig. 7: Reconstruction of view-dependent intensities. A corner reflector on a wall (a) is observed from multiple viewing directions in the "wall w/o window" dataset. The intensities of points on the wall decrease with lower incidence angles (b), and our model can reconstruct these view-dependent intensities with low reconstruction errors (c).

TABLE III: Ablation study on the inputs to the intensity network. For each configuration, we report the mean (MAE) and median (MedAE) absolute intensity reconstruction errors averaged over 10 repetitions, with standard deviations. Removing the SDF network noticeably decreases intensity reconstruction quality, whereas omitting SDF normals or the geometry feature has only a minor effect, suggesting that these inputs are less important for accurate intensity reconstruction. The errors are expressed in the same scale as the radar’s intensity measurements (see intensity range for each dataset in table II).

dataset	full		w/o SDF		w/o normals		w/o geo. fea.	
	MAE ( $\pm$ SD)	MedAE ( $\pm$ SD)	MAE ( $\pm$ SD)	MedAE ( $\pm$ SD)	MAE ( $\pm$ SD)	MedAE ( $\pm$ SD)	MAE ( $\pm$ SD)	MedAE ( $\pm$ SD)
Radar Forest	3.27 ( $\pm$ 0.06)	2.40 ( $\pm$ 0.05)	3.38 ( $\pm$ 0.03)	2.44 ( $\pm$ 0.03)	3.27 ( $\pm$ 0.05)	2.40 ( $\pm$ 0.04)	3.27 ( $\pm$ 0.06)	2.40 ( $\pm$ 0.04)
wall w/ window 1	2.65 ( $\pm$ 0.02)	2.00 ( $\pm$ 0.01)	2.72 ( $\pm$ 0.05)	2.06 ( $\pm$ 0.04)	2.65 ( $\pm$ 0.03)	2.02 ( $\pm$ 0.02)	2.66 ( $\pm$ 0.03)	2.01 ( $\pm$ 0.02)
wall w/ window 2	2.48 ( $\pm$ 0.01)	1.81 ( $\pm$ 0.01)	2.52 ( $\pm$ 0.03)	1.82 ( $\pm$ 0.02)	2.47 ( $\pm$ 0.02)	1.81 ( $\pm$ 0.01)	2.47 ( $\pm$ 0.02)	1.80 ( $\pm$ 0.02)
wall w/o window	2.81 ( $\pm$ 0.05)	2.09 ( $\pm$ 0.03)	2.83 ( $\pm$ 0.04)	2.13 ( $\pm$ 0.03)	2.82 ( $\pm$ 0.04)	2.12 ( $\pm$ 0.03)	2.86 ( $\pm$ 0.06)	2.13 ( $\pm$ 0.04)
SNAIL basketball court	4.92 ( $\pm$ 0.05)	2.73 ( $\pm$ 0.06)	5.13 ( $\pm$ 0.06)	2.87 ( $\pm$ 0.06)	4.98 ( $\pm$ 0.08)	2.77 ( $\pm$ 0.07)	4.97 ( $\pm$ 0.10)	2.76 ( $\pm$ 0.08)
SNAIL starlake tower	4.35 ( $\pm$ 0.14)	2.65 ( $\pm$ 0.08)	4.85 ( $\pm$ 0.02)	2.87 ( $\pm$ 0.03)	4.57 ( $\pm$ 0.08)	2.76 ( $\pm$ 0.04)	4.51 ( $\pm$ 0.10)	2.73 ( $\pm$ 0.06)

resolution typical of 3D radars, our method produces dense, smooth, and geometrically consistent reconstructions. In addition, it successfully captures view-dependent radar responses, enabling the model to explain not only where surfaces are, but also how they reflect energy. This joint modelling of geometry and intensity provides a richer and more physically meaningful scene representation than purely geometric reconstructions. However, performance notably depends on the quality of the input data. We further observe that common evaluation metrics may not fully capture reconstruction quality with sparse radar data. To provide a more faithful assessment, we therefore complement conventional metrics (completion, accuracy, F-score) with additional quantitative analyses (local surface smoothness, accuracy outlier ratio) as well as qualitative inspection, highlighting the limitations of current evaluation practices. Future work will focus on modelling radar-specific characteristics, such as multi-path reflections and the effects of a wide beam, to enable more physically accurate scene reconstruction.

#### REFERENCES

- [1] B. Mildenhall, P. P. Srinivasan, M. Tancik, J. T. Barron, R. Ramamoorthi, and R. Ng, "NeRF: Representing Scenes as Neural Radiance Fields for View Synthesis", *Commun. ACM*, vol. 65, no. 1, pp. 99–106, 2021.
- [2] S. Isaacson, P.-C. Kung, M. Ramanagopal, R. Vasudevan, and K. A. Skinner, "LONER: LiDAR Only Neural Representations for Real-Time SLAM", *IEEE Robot. Automat. Lett.*, vol. 8, no. 12, pp. 8042–8049, 2023.
- [3] X. Zhong, Y. Pan, J. Behley, and C. Stachniss, "SHINE-Mapping: Large-Scale 3D Mapping Using Sparse Hierarchical Implicit Neural Representations", in *Proc. IEEE Int. Conf. Robot. Automat.*, 2023, pp. 8371–8377.
- [4] S. Sun, M. Mielle, A. J. Lilienthal, and M. Magnusson, "3QFP: Efficient neural implicit surface reconstruction using Tri-Quadrees and Fourier feature Positional encoding", in *Proc. IEEE Int. Conf. Robot. Automat.*, 2024, pp. 4036–4044.
- [5] D. Borts et al., "Radar Fields: Frequency-Space Neural Scene Representations for FMCW Radar", in *Proc. ACM SIGGRAPH*, 2024, pp. 1–10.
- [6] T. Huang et al., "DART: Implicit Doppler Tomography for Radar Novel View Synthesis", in *Proc. IEEE/CVF Conf. Comput. Vis. Pattern Recognit.*, 2024, pp. 24 118–24 129.
- [7] J. Zhang, Z. Li, C. Wang, and B. Wen, "RF4D: Neural Radar Fields for Novel View Synthesis in Outdoor Dynamic Scenes". arXiv: 2505.20967.
- [8] W. Sheng, H. Liu, K. Fan, and P. Su, "GeoRF: Geometric Constrained RaDAR Fields", *IEEE Access*, vol. 13, pp. 78 391–78 402, 2025.
- [9] M. Rafidashti, J. Lan, M. Fatemi, J. Fu, L. Hammarstrand, and L. Svensson, "NeuRadar: Neural Radiance Fields for Radar Novel View Synthesis", in *Proc. IEEE/CVF Conf. Comput. Vis. Pattern Recognit.*, 2024, pp. 24 130–24 139.

- ance Fields for Automotive Radar Point Clouds”, in *Proc. IEEE/CVF Conf. Comput. Vis. Pattern Recognit. Workshops*, 2025, pp. 2479–2489.
- [10] Y. Wang, Q. Han, M. Habermann, K. Daniilidis, C. Theobalt, and L. Liu, “NeuS2: Fast Learning of Neural Implicit Surfaces for Multi-view Reconstruction”, in *Proc. IEEE/CVF Conf. Comput. Vis. Pattern Recognit.*, 2023, pp. 3272–3283.
- [11] A. Hornung, K. M. Wurm, M. Bennewitz, C. Stachniss, and W. Burgard, “OctoMap: An efficient probabilistic 3D mapping framework based on octrees”, *Auton. Robots*, vol. 34, no. 3, pp. 189–206, 2013.
- [12] A. Kramer and C. Heckman, “Radar-Inertial State Estimation and Obstacle Detection for Micro-Aerial Vehicles in Dense Fog”, in *Exp. Robot. Vol. 19*, 2021, pp. 3–16.
- [13] J. Behley and C. Stachniss, “Efficient Surfel-Based SLAM using 3D Laser Range Data in Urban Environments”, in *Proc. Robot. Sci. Syst.*, 2018.
- [14] K. Wang, F. Gao, and S. Shen, “Real-time Scalable Dense Surfel Mapping”, in *Proc. IEEE Int. Conf. Robot. Automat.*, 2019, pp. 6919–6925.
- [15] H. Edelsbrunner, D. Kirkpatrick, and R. Seidel, “On the shape of a set of points in the plane”, *IEEE Trans. Inf. Theory*, vol. 29, no. 4, pp. 551–559, 1983.
- [16] F. Bernardini, J. Mittleman, H. Rushmeier, C. Silva, and G. Taubin, “The ball-pivoting algorithm for surface reconstruction”, *IEEE Trans. Vis. Comput. Graph.*, vol. 5, no. 4, pp. 349–359, 1999.
- [17] M. Kazhdan, M. Bolitho, and H. Hoppe, “Poisson Surface Reconstruction”, in *Proc. Eurographics Symp. Geom. Process.*, 2006, pp. 61–70.
- [18] I. Vizzo, X. Chen, N. Chebrolu, J. Behley, and C. Stachniss, “Poisson Surface Reconstruction for LiDAR Odometry and Mapping”, in *Proc. IEEE Int. Conf. Robot. Automat.*, 2021, pp. 5624–5630.
- [19] Z. Han, H. Fang, Q. Yang, Y. Bai, and L. Chen, “Online 3D Reconstruction Based On Lidar Point Cloud”, in *Proc. Chin. Control Conf.*, 2023, pp. 4505–4509.
- [20] H. Oleynikova, Z. Taylor, M. Fehr, R. Siegwart, and J. Nieto, “Voxblox: Incremental 3D Euclidean Signed Distance Fields for on-board MAV planning”, in *Proc. IEEE/RSJ Int. Conf. Intell. Robots Syst.*, 2017, pp. 1366–1373.
- [21] I. Vizzo, T. Guadagnino, J. Behley, and C. Stachniss, “VDBFusion: Flexible and Efficient TSDF Integration of Range Sensor Data”, *Sensors*, vol. 22, no. 3, p. 1296, 2022.
- [22] L. Mescheder, M. Oechsle, M. Niemeyer, S. Nowozin, and A. Geiger, “Occupancy Networks: Learning 3D Reconstruction in Function Space”, in *Proc. IEEE/CVF Conf. Comput. Vis. Pattern Recognit.*, 2019, pp. 4455–4465.
- [23] M. Oechsle, S. Peng, and A. Geiger, “UNISURF: Unifying Neural Implicit Surfaces and Radiance Fields for Multi-View Reconstruction”, in *Proc. IEEE/CVF Conf. Comput. Vis. Pattern Recognit.*, 2021, pp. 5569–5579.
- [24] D. Yan, X. Lyu, J. Shi, and Y. Lin, “Efficient Implicit Neural Reconstruction Using LiDAR”, in *Proc. IEEE Int. Conf. Robot. Automat.*, 2023, pp. 8407–8414.
- [25] L. Yariv, J. Gu, Y. Kasten, and Y. Lipman, “Volume Rendering of Neural Implicit Surfaces”, in *Adv. Neural Inf. Process. Syst.*, 2021.
- [26] P. Wang, L. Liu, Y. Liu, C. Theobalt, T. Komura, and W. Wang, “NeuS: Learning Neural Implicit Surfaces by Volume Rendering for Multi-view Reconstruction”, in *Adv. Neural Inf. Process. Syst.*, 2021, pp. 27 171–27 183.
- [27] M. Wysocki, M. F. Azampour, C. Eilers, B. Busam, M. Salehi, and N. Navab, “Ultra-NeRF: Neural Radiance Fields for Ultrasound Imaging”, in *Proc. Med. Imaging Deep Learn.*, 2024, pp. 382–401.
- [28] M. Qadri, M. Kaess, and I. Gkioulekas, “Neural Implicit Surface Reconstruction using Imaging Sonar”, in *Proc. IEEE Int. Conf. Robot. Automat.*, 2023, pp. 1040–1047.
- [29] Y. Xie, G. Troni, N. Bore, and J. Folkesson, “Bathymetric Surveying With Imaging Sonar Using Neural Volume Rendering”, *IEEE Robot. Automat. Lett.*, vol. 9, no. 9, pp. 8146–8153, 2024.
- [30] Z. Lei, F. Xu, J. Wei, F. Cai, F. Wang, and Y.-Q. Jin, “SAR-NeRF: Neural Radiance Fields for Synthetic Aperture Radar Multi-View Representation”, *IEEE Trans. Geosci. Remote Sens.*, vol. 62, pp. 1–15, 2024.
- [31] N. Sugavanam and E. Ertin, “Neural Implicit Representations for 3D Synthetic Aperture Radar Imaging”, *IEEE Trans. Geosci. Remote Sens.*, vol. 62, pp. 1–15, 2024.
- [32] B. Mildenhall, P. Hedman, R. Martin-Brualla, P. P. Srinivasan, and J. T. Barron, “NeRF in the Dark: High Dynamic Range View Synthesis from Noisy Raw Images”, in *Proc. IEEE/CVF Conf. Comput. Vis. Pattern Recognit.*, 2022, pp. 16 169–16 178.
- [33] W.-T. Chen, W. Yifan, S.-Y. Kuo, and G. Wetzstein, “DehazeNeRF: Multi-image Haze Removal and 3D Shape Reconstruction using Neural Radiance Fields”, in *Proc. Int. Conf. 3D Vis.*, 2024, pp. 247–256.
- [34] W. E. Lorensen and H. E. Cline, “Marching cubes: A high resolution 3D surface construction algorithm”, *SIGGRAPH Comput. Graph.*, vol. 21, no. 4, pp. 163–169, 1987.
- [35] J. Huai, B. Wang, Y. Zhuang, Y. Chen, Q. Li, and Y. Han, “SNAIL radar: A large-scale diverse benchmark for evaluating 4D-radar-based SLAM”, *Int. J. Robot. Res.*, vol. 44, no. 12, pp. 1941–1958, 2025.
- [36] Q.-Y. Zhou, J. Park, and V. Koltun. “Open3D: A Modern Library for 3D Data Processing”. arXiv: 1801.09847.